Geophysical Journal International

Geophys. J. Int. (2012) **189,** 898–910 doi: 10.1111/j.1365-246X.2012.05432.x

Correcting atmospheric effects on InSAR with MERIS water vapour data and elevation-dependent interpolation model

Z. W. Li,[1] W. B. Xu,[1,2] G. C. Feng,[1] J. Hu,[1] C. C. Wang,[1] X. L. Ding[3] and J. J. Zhu[1]

[1]*School of Geosciences and Info-Physics, Central South University, Changsha* 410083, *Hunan, P.R. China. E-mail: zwli@csu.edu.cn*
[2]*King Abdullah University of Science and Technology, Thuwal* 23955, *Saudi Arabia*
[3]*Department of Land Surveying and Geo-Informatics, Hong Kong Polytechnic University, Hung Hom, Kowloon, Hong Kong, P.R. China*

Accepted 2012 February 22. Received 2012 February 22; in original form 2011 December 15

SUMMARY

The propagation delay when radar signals travel from the troposphere has been one of the major limitations for the applications of high precision repeat-pass Interferometric Synthetic Aperture Radar (InSAR). In this paper, we first present an elevation-dependent atmospheric correction model for Advanced Synthetic Aperture Radar (ASAR—the instrument aboard the ENVISAT satellite) interferograms with Medium Resolution Imaging Spectrometer (MERIS) integrated water vapour (IWV) data. Then, using four ASAR interferometric pairs over Southern California as examples, we conduct the atmospheric correction experiments with cloud-free MERIS IWV data. The results show that after the correction the rms differences between InSAR and GPS have reduced by 69.6 per cent, 29 per cent, 31.8 per cent and 23.3 per cent, respectively for the four selected interferograms, with an average improvement of 38.4 per cent. Most importantly, after the correction, six distinct deformation areas have been identified, that is, Long Beach–Santa Ana Basin, Pomona–Ontario, San Bernardino and Elsinore basin, with the deformation velocities along the radar line-of-sight (LOS) direction ranging from -20 mm yr^{-1} to -30 mm yr^{-1} and on average around -25 mm yr^{-1}, and Santa Fe Springs and Wilmington, with a slightly low deformation rate of about -10 mm yr^{-1} along LOS. Finally, through the method of stacking, we generate a mean deformation velocity map of Los Angeles over a period of 5 yr. The deformation is quite consistent with the historical deformation of the area. Thus, using the cloud-free MERIS IWV data correcting synchronized ASAR interferograms can significantly reduce the atmospheric effects in the interferograms and further better capture the ground deformation and other geophysical signals.

Key words: Image processing; Satellite geodesy; Radar interferometry; Creep and deformation; Wave propagation.

1 INTRODUCTION

Interferometric synthetic aperture radar (InSAR) is a very powerful technology for earth observations due to its all-weather and day-and-night imaging capability, wide spatial coverage, fine resolution and competitive accuracy (Massonnet & Feigl 1998; Rosen *et al.* 2000). It has been widely applied for mapping earth's topography (Zebker & Goldstein 1986; Madsen *et al.* 1993), and for monitoring ground deformation associated with, for example, earthquakes (Massonnet *et al.* 1994; Feng *et al.* 2010, 2011), tectonic contraction (Bawden *et al.* 2001), hydrothermal/magmatic fluid migration (Wicks *et al.* 1998), underground mining (Ge *et al.* 2007), underground water pumping (Galloway *et al.* 1998; Fruneau *et al.* 2005), oil extraction (Fielding *et al.* 1998), and land reclamation (Ding *et al.* 2004). Such kinds of measurements are however always affected by atmospheric propagation delay (e.g. Goldstein 1995; Zebker *et al.* 1997; Hanssen 1998; Li *et al.* 2003b, 2007; Ding *et al.* 2008). Zebker *et al.* (1997), for example, reported that a 20 per cent changes in the atmospheric relative humidity could introduce up to 10–14 cm errors in the measured ground deformations and 80–290 m errors in the derived topographic maps for perpendicular baselines ranging from 400 to 100 m. Atmospheric effects thus have been one of the limiting error sources in repeat-pass InSAR measurements.

A number of methods have been developed in the past years to model and correct atmospheric effects on InSAR (Li *et al.* 2003b; Ding *et al.* 2008). They can however be divided into four types: (1) stacking SAR interferograms (e.g. Zebker *et al.* 1997; Williams *et al.* 1998; Ferretti *et al.* 1999); (2) correlation analysis between interferograms or between interferometric phases and elevations (e.g. Beauducel *et al.* 2000; Fruneau & Sarti 2000; Remy *et al.* 2003; Chaabane *et al.* 2007); (3) permanent scatterer techniques (e.g. Ferretti *et al.* 2000; Hooper *et al.* 2004) and (4) calibration with external data such as ground meteorological data (e.g. Delacourt *et al.* 1998), GPS data (e.g. Li *et al.* 2006a; Li *et al.* 2006d), high-resolution meteorological model (e.g. Webley *et al.* 2004; Foster *et al.* 2006), Moderate Resolution Imaging Spectroradiometer

(MODIS) data (e.g. Li 2005; Li *et al.* 2005) and Medium Resolution Imaging Spectrometer (MERIS) data (e.g. Li *et al.* 2006c; Li *et al.* 2009; Xu *et al.* 2010). Stacking SAR interferograms will degrade the temporal resolution of InSAR measurements and probably mix useful geophysical signals, especially the transient signals. The method of correlation analysis however can only model and reduce the tropospheric noise that correlates within different interferograms or with elevation strongly, while the permanent scatterer techniques need a large number of images and don't work well when the atmospheric noises are similar to the useful geophysical signals in the spatial or temporal domain. Calibration methods have attracted increasing attention in recent years with the improvements of both the accuracy and the resolution of external data (e.g. Li 2005; Li *et al.* 2005; Li *et al.* 2006c; Puysségur *et al.* 2007; Ding *et al.* 2008; Li *et al.* 2009). Of the external data used in the calibration methods, the MERIS Precipitable Water Vapour (PWV) data have a spatial resolution up to 0.3 km, much higher than that of the other data sources, and an accuracy close to that of GPS (with a rms difference of about 1.1 mm) but higher than that of the MODIS data (Li *et al.* 2003a, 2006b;). In addition, as both the MERIS PWV data and Advanced Synthetic Aperture Radar (ASAR) instruments are onboard ENVISAT, the respective images have an almost identical propagation path and can be acquired simultaneously. Thus, the MERIS PWV data are very promising for correcting atmospheric effects in ASAR interferograms. Li *et al.* (2006b) first assessed the potential of using MERIS water vapour products to correct ASAR interferometric measurements. Subsequently, Li *et al.* (2006c) and Ding *et al.* (2008) reported the use of MERIS PWV data to correct ASAR interferograms over Los Angeles and Hong Kong area, respectively. For more advanced InSAR atmospheric corrections with MERIS data, Puysségur *et al.* (2007) proposed the integration of MM5 model (The Fifth-Generation mesoscale meteorological model developed by National Center for Atmospheric Research/Pennsylvania State University) and MERIS data, while Li *et al.* (2009) suggested the combined use of the MODIS and MERIS data. However, the improvement by adding MERIS data to the MM5 model is not significant, and the results of the combined use of the MODIS and MERIS data are similar to that obtained by using MERIS data alone or by GPS/MODIS integration. Williams *et al.* (1998) demonstrated that in addition to the accuracy and density of the external data, the interpolation model adopted to construct atmospheric delay map is also crucial for InSAR atmospheric correction. Although there are a couple of researches that use MERIS water vapour data to correct ASAR interferograms, the interpolation models adopted are generally very common, like the (improved) inverse distance weighted (IDW) interpolator (Li *et al.* 2006c; Li *et al.* 2009), the Simple Kriging (Ding *et al.* 2008), etc. The elevation-dependent nature of water vapour delay is not well considered in these models.

In this paper, we present an elevation-dependent interpolator to construct atmospheric delay map with MERIS data and to correct its effects on InSAR measurements over Los Angeles area. The accuracy of the correction will be assessed with the GPS data of the South California Integrated GPS Network (SCIGN), one of the densest continuous GPS networks in the world. The corrected interferograms will help us to better evaluate the recent ground deformation over Los Angeles. Although the deformation of Los Angeles has been studied extensively with InSAR technology, to our knowledge, the studies mainly focus on the deformation before 2006 (Bawden *et al.* 2001; Watson *et al.* 2002; Lanari *et al.* 2004; Li *et al.* 2006c; Samsonov *et al.* 2007). This work mainly uses the ASAR data acquired from 2004 to 2009 and thus will provide us improved knowledge about the ground deformation in this area. The paper is organized as follow: in Section 2, the MERIS water vapour data are introduced, followed by the discussion of the elevation-dependent interpolator in Section 3. The actual InSAR atmospheric corrections, accuracy assessments and ground deformation evaluations are discussed in Section 4. Finally, some conclusions are addressed in Section 5.

2 MERIS WATER VAPOUR DATA

Mounted together with the ASAR sensor on the European Space Agency's ENVISAT spacecraft, MERIS is a passive push-broom imaging spectrometer that measures the reflected solar radiation from the Earth's surface and clouds. MERIS instrument's field-of-view is 68.5°, generally covering a swath of 1150 km at a nominal altitude of 800 km and allowing global coverage in two or three days. MERIS observations are performed in 15 programmable spectral bands, ranging from the visible to the near-infrared (390–1040 nm). Two out of the 15 spectral bands in the near-infrared, one within the absorption band (885 nm) and the other outside the absorption band (900 nm), are used for remote sensing of water vapour content based on the differential absorption method. The water vapour content thus estimated is above land or ocean surface in cloud-free condition or above the highest cloud level in cloudy condition. MERIS final near-infrared water vapour products are provided at two nominal spatial resolutions, that is, 0.3 km for full resolution model and 1.2 km for reduced resolution mode (ESA 2006).

Bennartz & Fischer (2001) reported that the theoretical accuracy of water vapour retrieval from MERIS could be as high as 1.7 mm under cloud-free condition over land. Li *et al.* (2006b) conducted spatial-temporal comparisons among MERIS, GPS and Radiosonde PWVs and assessed the feasibility of applying MERIS PWV to correct atmospheric effects on ASAR interferometric measurements. The results showed ∼1.1 mm agreement between MERIS and GPS/Radiosonde PWV products in terms of standard deviation, and confirmed the great potential for correcting ASAR interferograms with MERIS data. In addition to higher accuracy, better spatial resolution, synchronized acquisition and almost identical propagation path with ASAR makes the MERIS water vapour product very competitive for correcting ASAR interferograms (Li *et al.* 2009). The main limitation of MERIS water vapour measurements is the sensitivity to the presence of clouds.

In this study, we use the reduced resolution MERIS water vapour products. The cloud mask products are also provided. In order for the MERIS PWV measurements to be useable for correcting ASAR interferograms, the cloud mask product must show a high probability, for example, 99 per cent, that the sky is clear (Li *et al.* 2006b; Xu *et al.* 2010). For the purpose of atmospheric delay correction, the MERIS PWV must be converted to wet zenith delay (WZD)

$$\mathrm{WZD} = \prod \cdot \mathrm{PWV}, \tag{1}$$

where the mapping scale factor $\prod$ is a dimensionless parameter given by (Bevis *et al.* 1994)

$$\prod = 10^{-6} \cdot \rho \cdot R_{\mathrm{v}} \cdot \left[\frac{k_3}{T_{\mathrm{m}}} + k_2 - w \cdot k_1 \right], \tag{2}$$

where ρ is the density of the liquid water, R_{v} is the specific gas constant for water vapour, k_1, k_2 and k_3 are the atmospheric refractivity constants, and w is the mass ratio of water vapour molecule to dry air molecule. T_{m} is the weighted mean temperature of the

troposphere

$$T_{\mathrm{m}} = \frac{\int (e/T) \cdot \mathrm{d}h}{\int (e/T^2) \cdot \mathrm{d}h}, \tag{3}$$

where e is the partial pressure of water vapour, T is the absolute temperature and h is the height along atmospheric profile.

The estimation of T_{m} based on eq. (3) is generally difficult. To approximate T_{m} with surface temperature T_0, Bevis *et al.* (1994) investigated the relationship between T_{m} and T_0 by analysing a large number of radiosonde data of North America, and found a strong linear correlation

$$T_{\mathrm{m}} = 70.2 + 0.72 \cdot T_0 \tag{4}$$

with an rms error of about 4.7 K.

Assuming that a surface temperature $T_0 = 300$K and a MEIRS water vapour content PWV = 2.0 cm, an error of 4.7 K in T_{m} will cause an uncertainty of 0.099 in the mapping scale factor $\prod$ based on eq. (2), and this finally will introduce an error of about 1.98 mm to the estimated WZD based on eq. (1). Thus, it is neglectable. In this study, we will use eqs. (1), (2) and (4) to convert MERIS PWV to WZD. The surface temperature T_0 in eq. (4) is interpolated by the IDW interpolator and the measured temperatures at the SCIGN GPS sites equipped with meteorological sensors.

3 ELEVATION-DEPENDENT INTERPOLATION MODEL OF WET DELAY

There are mainly three elevation-dependent interpolators of wet delay proposed in the past decades. They are the Best Linear Unbiased Estimator in combination with the water vapour Height Scaling Model (Emardson & Johansson 1998), the Best Linear Unbiased Estimator coupled with the Elevation-dependent Covariance Model (Li *et al.* 2006a), and the Simple Kriging with varying local means (SKlm) estimator in conjunction with the Baby semi-empirical model (Li *et al.* 2006d). In the third elevation-dependent interpolator (called SKlm+Baby hereinafter), the Baby semi-empirical model (Baby *et al.* 1988) is used to model the elevation-dependent component of the water vapour delay. As the Baby semi-empirical model is only reference to one meteorological station and the model itself has an uncertainty of up to several centimetres (Li *et al.* 2008a), the elevation-dependent component of water vapour delay is difficult to model accurately. This degrades the accuracy of the SKlm+Baby interpolator. To account for this, more recently, Xu *et al.* (2011a) substitute the inaccurate Baby semi-empirical model with the Onn water vapour model (Onn & Zebker 2006), and formulate a revision to the SKlm+Baby interpolator

$$Z^*_{\mathrm{SKlm}}(u) = \sum_{i=1}^{n} w_i^{\mathrm{SK}} [Z(u_i) - m^*_{\mathrm{SK}}(u_i)] + m^*_{\mathrm{SK}}(u), \tag{5}$$

where $Z^*_{\mathrm{SKlm}}(u)$ denotes the interpolated water vapour delay at location u; $Z(u_i)$ represents the measured water vapour delay at location u_i; n is the number of measured water vapour delays used for the interpolation; w_i^{SK} are the Kriging weights to be determined; $m^*_{\mathrm{SK}}(u_i)$ denotes the known varying means (i.e. the elevation-dependent component of water vapour delay) at locations u_i and is estimated from the Onn water vapour model:

$$m^*_{\mathrm{SK}}(u_i) = Ce^{-\alpha h} + h\alpha Ce^{-\alpha h} + Z_{\min}, \tag{6}$$

where C is proportional to the amount of water vapour delay measured at sea level; α is the delay rate of the vertical water vapour profile; h is the ground height and $Z_{\min}$ is the water vapour delay at the highest location. C, α and $Z_{\min}$ can be estimated by regression analysis of the water vapour delay samples with respect to the ground heights.

The Kriging weights w_i^{SK} in eq. (5) can be obtained by solving the following system (Goovaerts 1997; Li *et al.* 2006d)

$$\sum_{i=1}^{n} w_i^{\mathrm{SK}} C_R(u_i - u_j) = C_R(u_i - u), \quad j = 1, \ldots, n, \tag{7}$$

where C_{R} is the covariance function of the residual water vapour delay $R(u) = Z(u) - m^*_{\mathrm{SK}}(u)$.

Cross-validation analyses with the GPS wet delays measured by SCIGN show that the rms of the SKlm + Onn interpolator is only 0.55 cm, while those of the previous three elevation-dependent interpolators amount to 0.77, 1.11 and 1.49 cm (Xu *et al.* 2011a). Thus, the SKlm + Onn interpolator represents significant improvements over other elevation-dependent ones. In this study, we will use the SKlm + Onn interpolator to construct the atmospheric delay map with the MERIS PWV measurements.

4 CASE STUDY: LOS ANGELES, SOUTH CALIFORNIA

4.1 Study area and SAR data

The Los Angeles basin is located in Southern California, USA. It includes a number of active faults and is subjected to complex ground deformation related to tectonic movement and anthropogenic activities (Bock & Williams 1997; Watson *et al.* 2002). It is bounded by the Pacific Ocean to the west and southwest and is with very high water vapour content. Most important, it is well covered by the SCIGN (Hudnut *et al.* 2001), which makes it very suitable for InSAR atmospheric correction study.

In this case study, four temporally consecutive descending ASAR interferograms (Frame: 2925; Track: 170) covering Los Angeles are used for the atmospheric correction experiments. The basic parameters of the interferograms (Ifm for short) are listed in Table 1. The corrected interferograms will be used to evaluate the ground deformation of Los Angeles from 2004 August 7 to 2009 August 1.

The SCIGN GPS data at the ASAR acquisition times are downloaded from website http://www.scign.org and then differentiated to get the 3-D surface deformations. The 3-D deformations at each GPS site are then projected to the radar line-of-sight (LOS) direction (unit vector: east = 0.379, north = −0.097, up = 0.921) for comparisons with InSAR.

4.2 D-InSAR processing

We use GAMMA software to process the four interferometric pairs. Precise DORIS orbit data from European Space Agency (ESA) are used to reduce baseline errors and assist image co-registration and flat earth phase removal. The Digital Elevation Model (DEM) from the Shuttle Radar Topography Mission (SRTM) is used to remove the topographic contribution in the interferograms. The uncertainty of the DEM is about 7 m (Farr & Kobrick 2000) and can introduce phase errors of about 0.83, 0.34, 0.98 and 0.52 radians in the four interferograms, respectively (Table 1), which are comparable or just slightly above the typical phase noise level of about 0.75 radians in InSAR pairs (Hanssen 2001). We thus do not consider them in the following analysis. The interferometric pairs are processed by multi-looking operation with 20 pixels in azimuth and

Table 1. Basic parameters of ASAR interferograms used.

	Master	Slave	$B_\perp$ (m)	σ^* (radians)	Time Span (days)
Ifm1	2004 August 7	2005 October 1	−189 to −169	0.83	420
Ifm2	2005 October 1	2007 October 6	72 to 76	0.34	735
Ifm3	2007 October 6	2009 May 23	192 to 204	0.98	595
Ifm4	2009 May 23	2009 August 1	−107 to −101	0.52	70

*σ denotes the phase error induced by the SRTM height uncertainty.

4 pixels in range directions to get a final resolution of about 80 m by 80 m. To suppress noise, the interferograms are filtered with the improved Goldstein filter (Li *et al.* 2008b) and then unwrapped by the branch-cut method with the coherence threshold set to be 0.55 (Goldstein *et al.* 1988). The unwrapped interferograms are then mapped into LOS direction's ground deformation/atmospheric path delay, geocoded to the UTM projection.

4.3 Wet delay map construction

The synchronized cloud-free MERIS water vapour data are exploited to construct the atmospheric delay grids using the elevation-dependent interpolator described in Section 3. Taking into consideration the atmospheric delay correction in the next step, the atmospheric delay grids are constructed in the same space with the ASAR interferograms. More specifically, the procedures to construct the atmospheric delay grids include:

(1) resample the external DEM to the space of the geocoded and projected interferogram;
(2) calculate the mapping scale factor Π with eq. (2) and convert the MERIS PWVs into WZDs with eq. (1). The calculated WZDs set are then trimmed by the coverage of the ASAR interferogram;
(3) regress the model parameters in the Onn model with the derived elevation information in Step 1 and the WZD samples in Step 2;
(4) use the regressed model parameters in Step 3, the derived elevation information in Step 1, and eq. (6) to construct the elevation-dependent water vapour delay grids;
(5) determine the Kriging weights by eq. (7) with the 'flattened' water vapour delays (i.e. the water vapour delays after removing the elevation-dependent component) at the water vapour delay grids;
(6) use eq. (5) to construct the water vapour delay grids.

Fig. 1 shows the scatter plots of the MERIS WZD samples and the regressed Onn models for the five SAR acquisition dates. The regressed model parameters are shown in Table 2. We can see from Fig. 1 that for all the five dates the WZDs decrease with the elevations and on average can be approximated by the Onn models.

4.4 Atmospheric correction

4.4.1 Interferogram: 2004 August 7–2005 October 1

The WZD maps calculated above are converted into the radar LOS direction with the mapping function $1/\cos\theta$, where θ is the pixel-based incidence angle. The converted WZD maps are then differentiated and used to correct the interferograms listed in Table 1.

Fig. 2 shows the unwrapped phase, the modelled differential water vapour delay and the corrected phase for the interferogram 2004 August 7–2005 October 1 (i.e. Ifm1). They are overlaid on the shaded relief map of Los Angeles for better visualization and comparisons. The time span of this interferogram is 420 d. We anticipate some deformation existed throughout this period, which will be analysed in Section 4.5. It is clear that the negative signals (i.e. the ground surface moves away from the satellite) in northwest and the positive signals in southeast of Ifm1 (Fig. 2a) have been largely removed (Fig. 2c). The phase variations decrease from 4.86 to 1.77 radians in terms of standard deviation after applying the correction, which renders the corrected interferogram much flatter. Fig. 3 shows the comparisons of the ground deformations measured by InSAR and GPS in the radar LOS direction. Note that the GPS stations involved are listed in Table S1. It is clear from Fig. 3 that after applying the correction, the relatively large negative (around −40 mm) and positive (around 20 mm) ground deformations measured using InSAR without correction are decreased to around −10 mm, which are very consistent in trend with those by GPS. Quantitative results show that the RMS differences between the InSAR and GPS measurements drop from 2.3 to 0.7 cm after the correction. Thus, an improvement of about 69.6 per cent has been achieved.

4.4.2 Interferogram: 2005 October 1–2007 October 6

Fig. 4 shows the corrected results for interferogram 2005 October 1–2007 October 6 (i.e. Ifm2). The unwrapped phase, the modelled differential water vapour delay and the corrected phase are also superimposed on the shaded relief map. According to GPS measurements, the ground surface moves away from the satellite (defined as negative, see the conventions in Fig. 2), while we can clearly distinguish two positive deformation areas in Fig. 4(a) that are indicated by black rectangles. The positive signals in the two areas are greatly mitigated after applying the atmospheric correction (Fig. 4c). The phase variation of the unwrapped interferogram is about 3.04 radians. The equivalent of the corrected interferogram is about 2.58 radians. The rms differences between the InSAR and GPS measurements in LOS direction decrease from 1.16 to 0.83 cm (Fig. 5), indicating an improvement of 29 per cent. For reference, the GPS stations involved in the comparisons are listed in Table S1.

4.4.3 Interferogram: 2007 October 6–2009 May 23

The unwrapped phase, the modelled differential water vapour delay and the corrected phase for interferogram 2007 October 6–2009 May 23 (i.e. Ifm3) are shown in Fig. 6(a)–(c), respectively. It is clear that the negative signals in the eastern portion of the interferogram have been largely removed. The phase variation falls from 4.53 to 2.24 radians after applying the correction. The rms differences between the InSAR and GPS measurements in LOS direction decrease from 1.29 to 0.88 cm (Fig. 7), representing an improvement of 31.8 per cent. Please refer Table S1 for the GPS stations involved in the comparisons.

4.4.4 Interferogram: 2009 May 23–2009 August 1

Fig. 8 shows the unwrapped phase, the modelled differential water vapour delay and the corrected phase for interferogram 2009 May

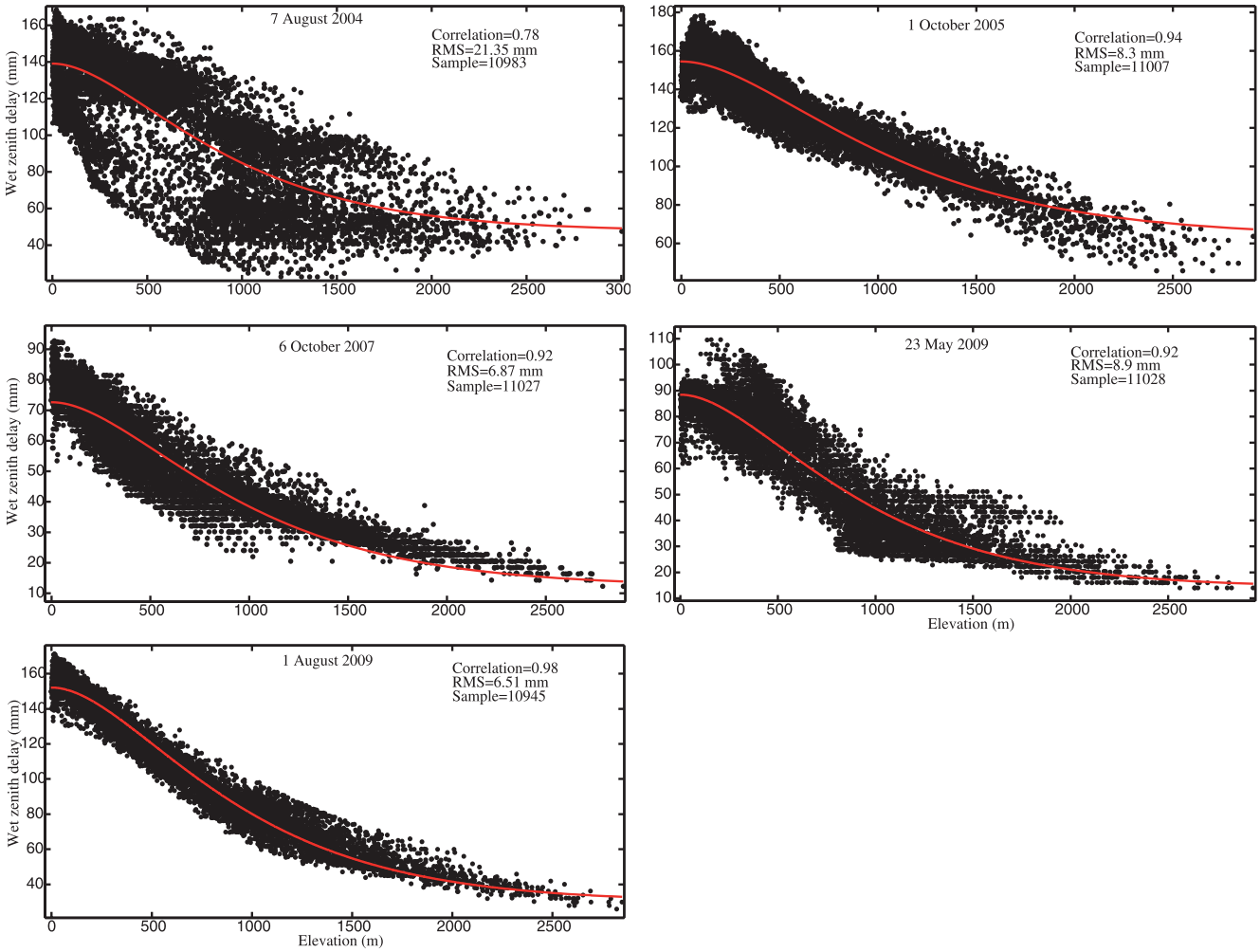

Figure 1. Regression of the Onn water vapor delay model.

Table 2. Regressed model parameters for the Onn model.

Date	C (mm)	α (km^{-1})	Z_{min} (mm)
2004 August 7	91.5	1.996	49.1
2005 October 1	90.8	1.712	67.3
2007 October 6	60.4	1.900	13.9
2009 May 23	74.3	1.985	15.7
2009 August 1	122.3	1.992	32.9

23–2009 August 1 (i.e. Ifm4). In Fig. 8(a), an apparent linear deformation trend runs across the whole image. After applying the correction, it is clear that the linear trend across the whole image has been largely removed. The positive phases around the summit of the San Gabriel Mountains however are over-corrected and become negative, while the negative phases in the middle and south of the interferogram are largely compensated. The phase variation decreases from 2.93 to 1.85 radians after applying the correction. The rms differences between the InSAR and GPS measurements in LOS direction decrease from 0.86 to 0.66 cm (Fig. 9). Thus, an improvement of 23.3 per cent has been achieved after the correction. Note that the GPS stations involved in the comparisons are listed in Table S1.

4.5 Analysis and discussion

In this section, we focus on (1) the discussion of the performance of the atmospheric correction and (2) the analysis of the geophysical signals (due to tectonic movements and anthropogenic activities) revealed by the interferograms after applying the corrections.

(1) In Ifm1, the Santa Ana basin shows a positive deformation (i.e. the ground surface moves toward the satellite), but the apparent uplift signals drop significantly after the atmospheric correction, although a portion of the positive signals still exist (Fig. 2c). The result is not agreeable with the GPS measurements, which reveal a negative deformation in this area (i.e. the ground surface moves away from the satellite). After atmospheric correction, the positive deformation in the east and the negative deformation in the northwest are largely removed. The corrected ground deformation, almost ranging between −20 and 0 mm, are pretty consistent with the LOS projected GPS measurements. These are also similar to the work of Watson *et al.* (2002) who found up to 56 mm LOS deformation in the Santa Ana basin from spring to autumn and a rather smaller deformation for a whole year. We also note that an uplift of ∼20 mm is observed in the San Bernardino area during this period. This could be caused by the high run-offs and resultant recharge from the San Gabriel and San Bernardino Mountains.

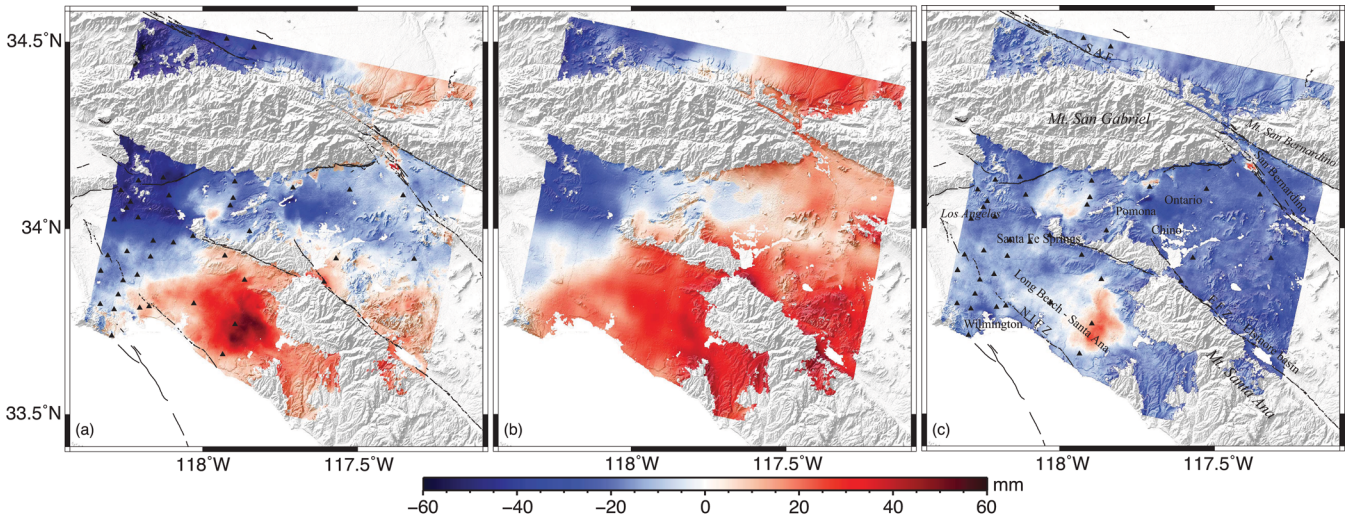

Figure 2. Atmospheric correction for interferometric pair of 2004 August 7 and 2005 October 1. (a) Original interferogram; (b) differenced wet delay map along LOS direction derived from MERIS data and elevation-dependent interpolator; (c) corrected interferogram. Note that negative implies the ground surface moves away from the satellite and positive towards the satellite. Black triangles denote the locations of the SCIGN GPS stations (ibid).

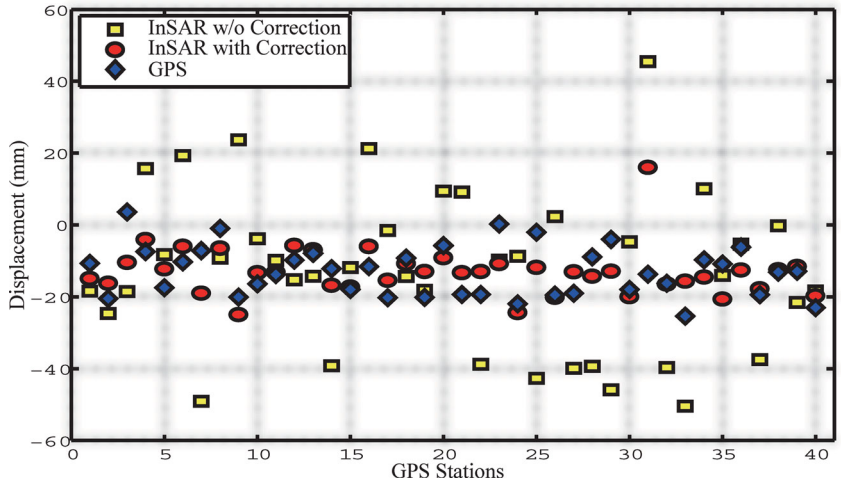

Figure 3. Comparisons of LOS deformations measured by InSAR and GPS before and after the atmospheric correction (interferometric pair of 2004 August 7 and 2005 October 1)

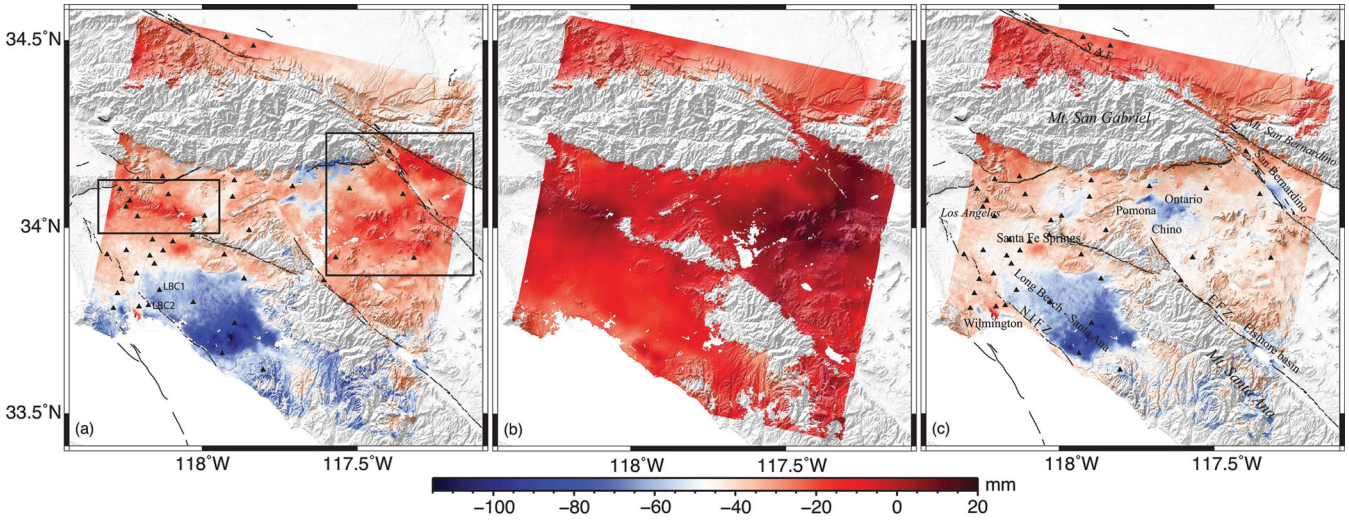

Figure 4. Atmospheric correction for interferometric pair of 2005 October 1 and 2007 October 6. (a) Original interferogram; (b) differenced wet delay map along LOS direction derived from MERIS data and elevation-dependent interpolator; (c) corrected interferogram.

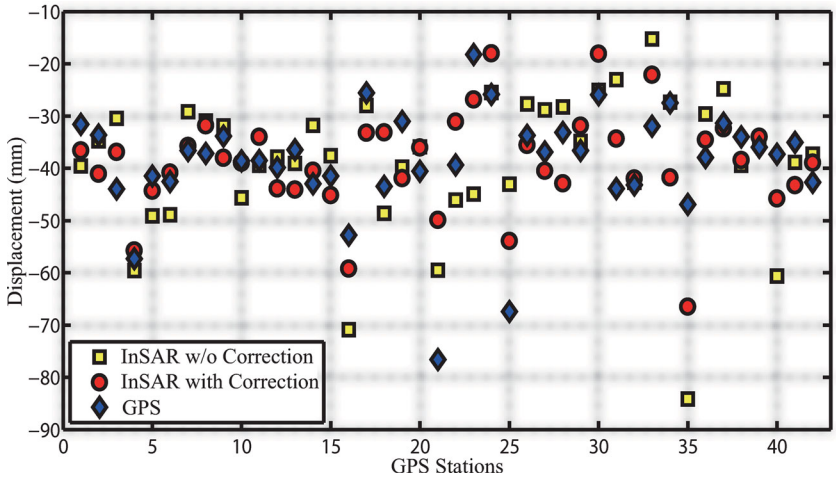

Figure 5. Comparisons of LOS deformations measured by InSAR and GPS before and after the atmospheric correction (interferometric pair of 2005 October 1 and 2007 October 6)

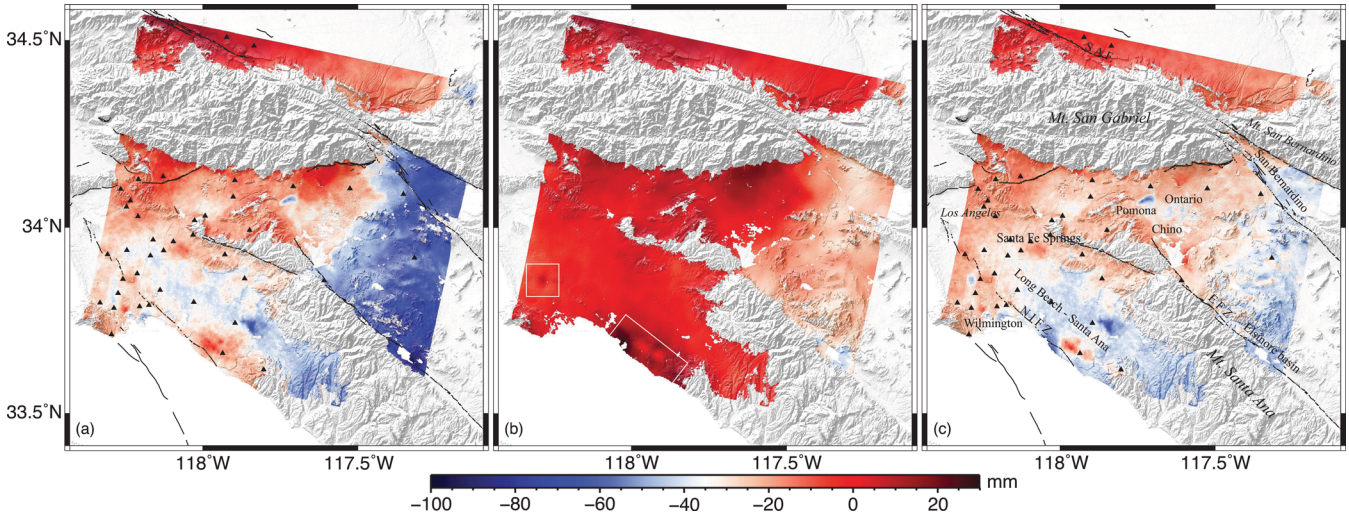

Figure 6. Atmospheric correction for interferometric pair of 2007 October 6 and 2009 May 23. (a) Original interferogram; (b) differenced wet delay map along LOS direction derived from MERIS data and elevation-dependent interpolator; (c) corrected interferogram.

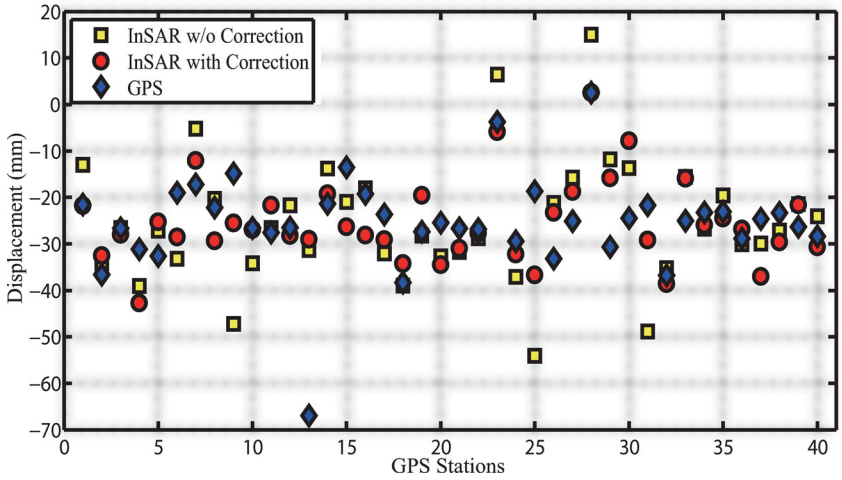

Figure 7. Comparisons of LOS deformations measured by InSAR and GPS before and after the atmospheric correction (interferometric pair of 2007 October 6 and 2009 May 23)

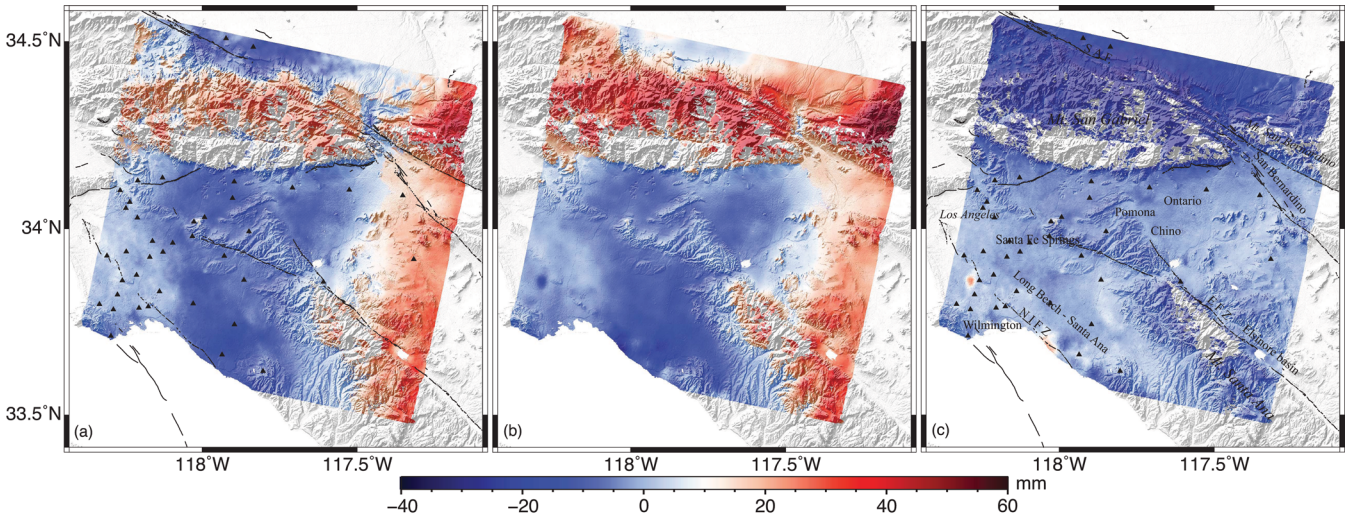

Figure 8. Atmospheric correction for interferometric pair of 2009 May 23 and 2009 August 1. (a) Original interferogram; (b) differenced wet delay map along LOS direction derived from MERIS data and elevation-dependent interpolator; (c) corrected interferogram.

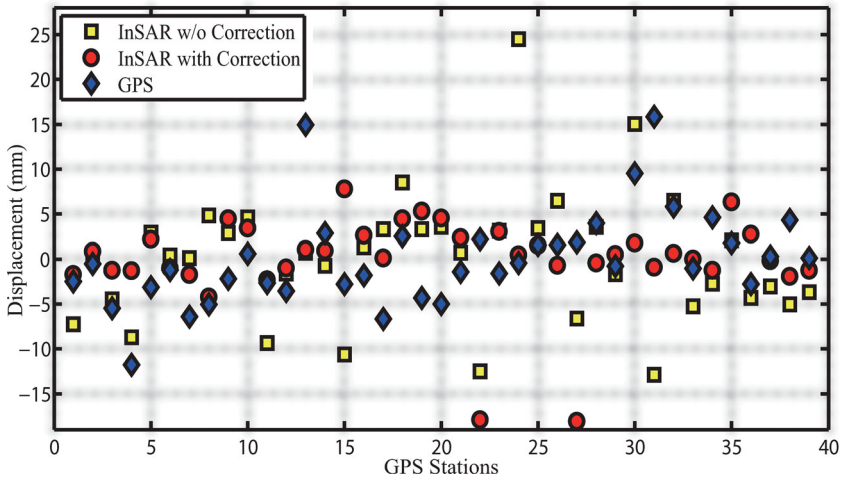

Figure 9. Comparisons of LOS deformations measured by InSAR and GPS before and after the atmospheric correction (interferometric pair of 2009 May 23 and 2009 August 1)

Lu & Danskin (2001) reported that the recharge in this area has caused up to 70 mm uplift within 8 months.

(2) For the long time span Ifm2, we can easily find four deformation areas, that is, Wilmington, Long Beach–Santa Ana basin, Pomona–Ontario and San Bernardino. According to the previous work (Watson *et al.* 2002; Lanari *et al.* 2004; Argus *et al.* 2005), the deformation in these areas are related to oil or groundwater withdrawal. Located along the Newport-Inglewood Fault Zone (NIFZ), the Long Beach–Santa Ana basin was found in previous work with a long-term subsidence of 12 mm yr^{-1} and seasonal deformation of 55 mm in vertical and 7 mm in horizontal direction, but bounded to the NIFZ (Bawden *et al.* 2001). In our study, the most obvious deformation is found located on the Santa Ana area and on the northwest part of the basin. Both the original (Fig. 4a) and the corrected interferograms (Fig. 4c) reveal these geophysical phenomena. It is interesting when comparing the deformation at the two very close GPS sites of LBC1 and LBC2 (referring Fig. 4a for their locations), which are located on either side of the NIFZ. The site of LBC1 is located on the east of the NIFZ, where the deformation is related to groundwater withdrawal in the basin, and thus it is with very large deformation. Although in the west, the NIFZ impedes groundwater flow to the east and the water table could be maintained, and therefore the LBC2 is only with subtle deformation. The small uplift in the Wilmington area is mainly due to the injection of gases after the oil withdrawal (Bawden *et al.* 2001). Like most of the other researches, we also detect an obvious subsidence in the Pomona–Ontario area. The subsidence is due to the ground water pumping from 1996 to present, and we tend to believe that such a long-term subsidence has triggered a permanent non-elastic deformation in the aquifer system (Xu *et al.* 2011b). Regarding the San Bernardino area, the existence of atmospheric water vapour covers the true ground deformation signals (in Fig. 4a). The corrected interferogram (Fig. 4c), however, reveals that ground subsidence is predominant in the area.

(3) For Ifm3, the atmospheric effects are significant in the east and northwest part of the interferogram. After the correction, we can see that the interferogram is much flatter (Fig. 6c), and the magnitude of the deformation in the Long Beach–Santa Ana basin, the Pomona–Ontario and San Bernardino areas are much smaller than those in Ifm2. As Ifm2 covers almost two whole years while Ifm3 starts in October of 2007 and ends in May of 2009, the deformation results imply that the volume of ground water withdrawal

is very large in the summer and the resulting ground subsidence is very significant. Although in winter, the ground water recharge rates should be larger than that of the withdrawal, as the subsidence is somewhat compensated. Nevertheless, some mistakes still occur at the boundary between sea and land (see the area marked by white rectangular in Fig. 6). This should be the failure of distinguishing thin cloud with the official MERIS cloud mask. Using pair-wise logical method (Massonnet & Feigl 1995), we find that it is due to the presence of thin cloud on 2007 October 6. Similar problem also exists in the area marked by the white square in Fig. 6, which is however due to the presence of thin cloud on 2009 May 23.

(4) The linear phase trend in Ifm4 has been removed after the atmospheric correction (Fig. 8). This means that the trend is not due to inaccurate baseline. In the original interferogram (Fig. 8a), some positive deformation located near the crests of the San Gabriel and San Bernardino Mountains with a maximum of 60 mm can be distinguished. Since the temporal interval of Ifm4 is short and its spatial baseline is relatively low, such a deformation is implausible. Although after the correction, the deformation is around −20 mm, which is a little over-corrected. The possible error sources that contribute to the residual phases in upper part of Fig. 8(c) should be due to possible artefact in the MERIS product. Besides, we also identify some mistakes along the coast, which is mainly due to thin-cloud effect too.

4.6 Stacking of deformation map

As the four ASAR interferograms used in this study are temporally consecutive, using the stacking method (Sandwell & Price 1998), we can generate a deformation map with very long time span. Stacking can avoid the serious temporal decorrelation caused by the long time span and that the random noise can be reduced to $1/\sqrt{N}$, with $N = 4$ in this study. The disadvantage however lies in that additional errors may be introduced in the processing of each interferogram. Nevertheless, we generate a mean deformation velocity map for the time interval between 2004 August 7 and 2009 August 1, by stacking the above four corrected deformation maps. The result is shown in Fig. 10(a). For comparison, we also generate the interferogram spanning from 2004 August 7 to 2009 August 1 using the two-pass D-InSAR method as described in Section 4.2.

There is no need to do atmospheric correction for the D-InSAR map (Fig. 10b), since the phase variations are very small, except for those around the mountains, which will not affect the analysis. We first compare the differences between the results by stacking and by D-InSAR. As can be seen from the two maps, the stacking method shows more clear deformation signals than D-InSAR, although the deformation patterns are very similar. The stacked interferogram better reveals the deformation phenomena in the Pomona basin than the one generated by D-InSAR, where the deformation gradient has exceeded the maximum detectable gradient by D-InSAR (i.e. one fringe per pixel) and consequently causes serious decorrelation (Jiang *et al.* 2011). We tried to construct a 'bridge' that connects the centre area with the outside area to get the phase unwrapped, but were unable to get a reasonable solution.

It is clear from both maps that the area south of the SAF is moving away from the satellite during 2004 August 7 to 2009 August 1, with a mean velocity of about −15 mm yr^{-1}. According to the geometry of descending ASAR image, any uniform ground deformation is expected to be caused by the horizontal tectonic movement related to the biggest fault in the area, that is, the San Andreas fault, whose Mojave segment is located 50 km north of the

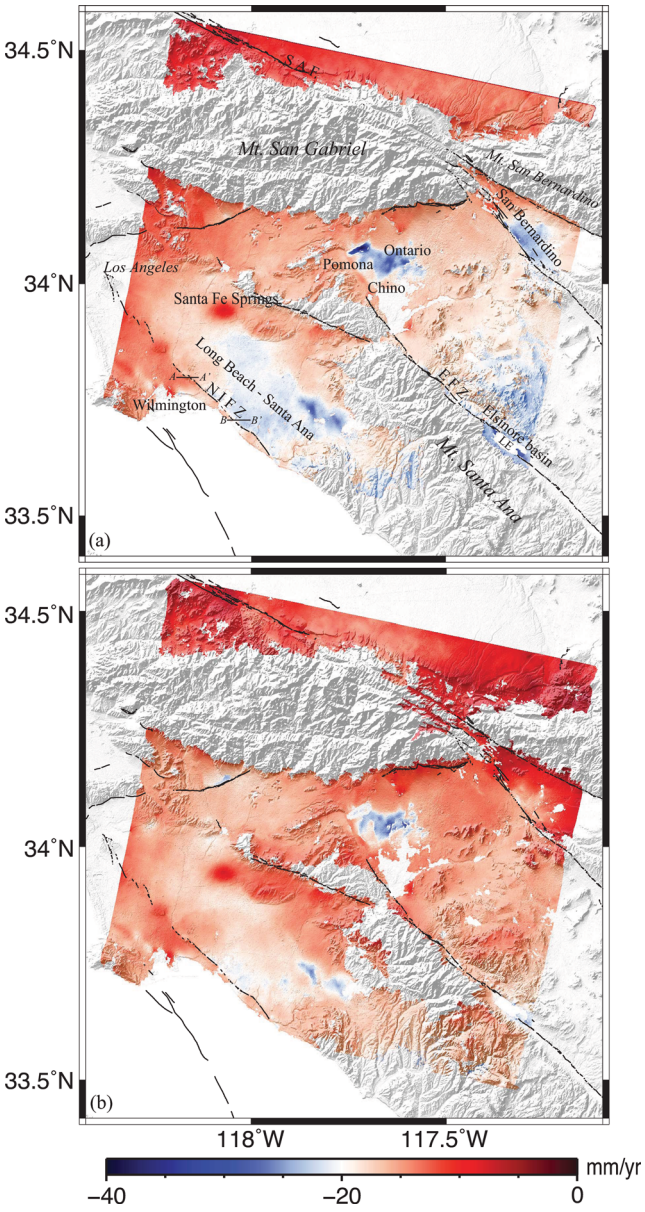

Figure 10. InSAR mean LOS deformation velocity map for the period between 2004 August 7 to 2009 August 1. (a) Stacking method, (b) D-InSAR method. Thin black lines indicate the mapped faults in this area, where EFZ, NIFZ and SAF stand for the Elsinore Fault Zone, the Newport-Inglewood Fault Zone, and the San Andreas Fault, respectively, and LE denotes the Lake Elsinore.

Los Angeles and trends west-northwest (Argus *et al.* 2005). Besides the uniform displacement, six significant local deformation patterns can be clearly identified in the area, including the Long Beach–Santa Ana basin (∼−25 mm yr^{-1} on average, with the maximum amount to ∼−30 mm yr^{-1}), the Pomona–Ontario area (∼−30 mm yr^{-1} on average, with the maximum amount to about −40 mm yr^{-1}), the San Bernardino area (∼−25 mm yr^{-1}), the Wilmington area (∼−10 mm yr^{-1}), the Santa Fe Springs area (∼−10 mm yr^{-1}) and the Elsinore basin (∼−25 mm yr^{-1}).

As the primary groundwater source of the Los Angeles area, the 400 km^2 Long Beach–Santa Ana Basin experiences severe seasonal oscillation caused by the anthropogenic activities, with subsidence from spring to autumn due to the groundwater extraction and uplift from autumn to spring due to the groundwater recharge (Bawden

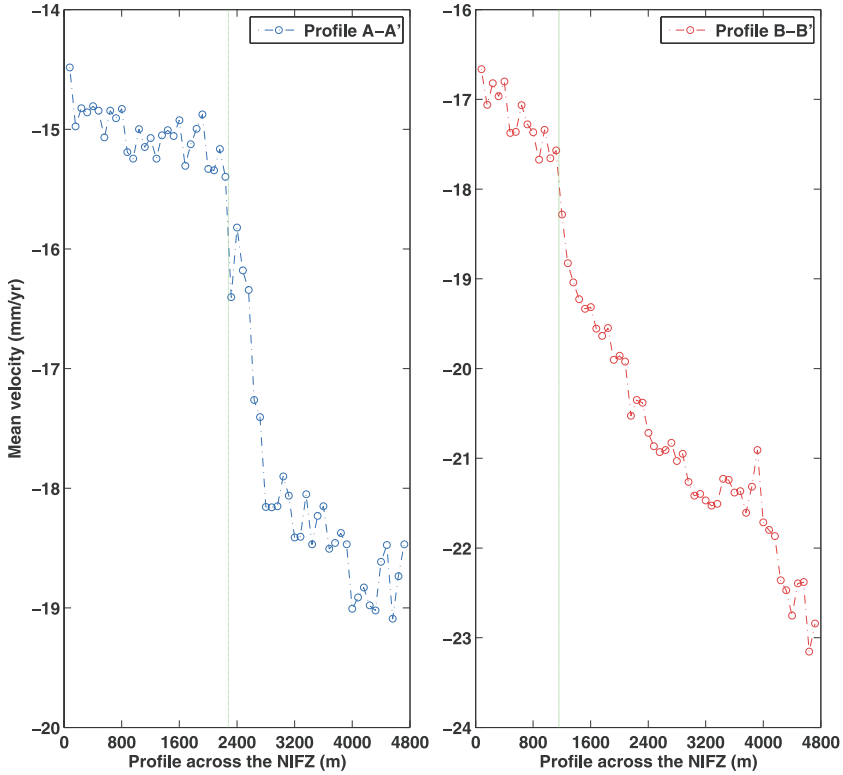

Figure 11. The profiles of the deformation velocity along A-A' and B-B'. The locations of A-A' and B-B' are shown in Fig. 10(a). Green line indicates the location of NIFZ.

et al. 2001; Lanari *et al.* 2004). As the time interval of our stacking results is only about 6 d short of 5 yr, most of the seasonal oscillations have been smoothed. However, by comparing with the other area, we can still detect little subsidence in this basin. This may be induced by the inelastic displacement that is transformed from the elastic displacement. It has been reported that the Long Beach–Santa Ana Basin is effectively isolated hydraulically by the NIFZ in the South (Bawden *et al.* 2001; Watson *et al.* 2002; Lanari *et al.* 2004). This phenomenon is confirmed by deformation velocity profiles across the NIFZ (Fig. 11). It is clear that there is a sudden drop of velocity in each of the profile, which corresponds to the locations of the fault traces.

In the previous studies, the results from InSAR and groundwater level data indicate that permanent subsidence in the Pomona–Ontario basin due to water pumping has occurred from 1993 to today (Ferretti *et al.* 2000; Bawden *et al.* 2001; Watson *et al.* 2002; Lanari *et al.* 2004). The continuous drawdown of water level could accelerate the occurrence of ground fissures and result in damage to existing infrastructure. We can see from Fig. 10(a) that the most dominant subsidence signal of up to 40 mm yr^{-1} is located in the Pomona area. According to the previous research, another obvious subsidence area used to concentrate on the Chino area (Bawden *et al.* 2001; Lanari *et al.* 2004), but now it extends northward into the Ontario area. These observations suggest that the current state of the Chino aquifer-system deformation is essentially inelastic, but needs more detailed investigation.

Deformation in the Wilmington and the Santa Fe Springs area may cause damages and pose threats to the infrastructure and lives there, because they are in the centre of a busy port and an industrial area, respectively. Using InSAR technology, we find that both of the areas show relative uplift along the LOS direction with regard to the surroundings areas. According to Pierce (1970), the surface uplift in the Wilmington field is mainly caused by the injection of saline water, while that in the Santa Fe Springs area may result from the recharge of the aquifers or the oil fields with water (Lanari *et al.* 2004).

The Elsinore basin is located in the southern end of the Santa Ana Watershed, with the main deformation areas located in the southeast and northwest part of this basin. To our knowledge, few research reports the deformation phenomena happened here using the InSAR technology. The Elsinore basin is one of the major sources of water supply in the Elsinore Valley Municipal Water District (EVMWD). Many installed groundwater-monitoring wells confirm that the groundwater level is declining (Elsinore basin groundwater advisory committee 2011). Groundwater pumping could be one of the problems that cause the ground subsidence. Lake Elsinore is located in the closed basin and shaped between the strands of the active Elsinore Fault Zone (EFZ), which extend from the northwest to the southeast across the basin. Another possible explanation for the subsidence is the aseismic strain accumulation of the active Elsinore Fault, although the slip rate is very low (Fialko 2006).

5 CONCLUSIONS

In this study, we develop an elevation-dependent atmospheric correction model for ASAR interferograms with the MERIS water vapour data. We conduct experiments to mitigate the atmospheric effects on four pairs of interferograms covering the great Los Angeles metropolitan area with the model. The result shows that using the model and the cloudless MERIS water vapour data to correct the synchronously acquired ASAR data, we can dramatically reduce the atmospheric effects on interferograms, and discriminate

some geophysical signals from water vapour effects. Comparing with LOS-projected GPS measurements, the accuracy of the corrected InSAR results are improved significantly. For the four pairs of selected interferograms, the rms differences between GPS and InSAR decreased by 69.6 per cent, 29 per cent, 31.8 per cent and 23.3 per cent, respectively, with an average of 38.4 per cent. In particular, after the correction, we can distinguish some deforming areas, four of which show obvious subsidence mainly due to groundwater withdrawals, that is, the Long Beach–Santa Ana basin (~ -25 mm yr^{-1}), the Pomona–Ontario area (~ -30 mm yr^{-1}), the San Bernardino area (~ -25 mm yr^{-1}) and the Elsinore basin (~ -25 mm yr^{-1}), while two of which, located in oil producing areas, experience slight relative uplift with respect to the surrounding areas, that is, the Wilmington area (~ -10 mm yr^{-1}) and the Santa Fe Springs area (~ -10 mm yr^{-1}). The results are consistent with the previous work (Watson *et al.* 2002; Bawden *et al.* 2001; Lanari *et al.* 2004).

However, some limitations and challenges remain in using this approach. First, although the MERIS official data provide geocoding information, cloud mask information and water vapour data, it is still not accurate enough to estimate the water vapour distributed in the boundary between the sea and land and to retrieve the water vapour due to thin cloud. Secondly, the general high cloud frequency affects the efficiency of the MERIS correction approach. Therefore, using GPS meteorological data or other meteorological measurements as a complement data with MERIS water vapour field is of great interest. Finally, although the proposed elevation-dependent correction model is easily modified to interpolate the water vapour data from GPS, MODIS and other meteorological measurements, it is still a simple one and needs to involve more realistic (albeit more complex) and robust geostatistical algorithms, for example, Co-Kriging, to model the dependence of water vapour delay on the elevation.

ACKNOWLEDGMENTS

This work was supported by the National Natural Science Foundation of China (Nos. 40974006 and 40774003), the Research Grants Council of the Hong Kong Special Administrative Region (Nos.: PolyU5155/07E), Program for New Century Excellent Talents in Universities (NCET-08–0570), and the Fundamental Research Funds for the Central Universities (No. 2011JQ001). The images are provided by the ESA under Category 1 User Projects (AO-4458 and 4914). We are grateful to Prof. Duncan Agnew and two anonymous reviewers whose constructive comments improve the quality of manuscript greatly. Several figures were produced using the Generic Mapping Tools (Wessel & Smith 1998).

REFERENCES

Argus, D.F., Heflin, M.B., Peltzer, G., Crampe, F. & Webb, F.H., 2005. Interseismic strain accumulation and anthropogenic motion in metropolitan Los Angeles, *J. geophys. Res.,* **110,** B04401, doi:10.1029/2003JB002934.

Baby, H.B., Gole, P. & Lavergnat, J., 1988. A model for the tropospheric excess path length of radio waves from surface meteorological measurements, *Radio Sci.,* **23**(6), 1023–1038.

Bawden, G.W., Thatcher, W., Stein, R.S., Hudnut, K.W. & Peltzer, G., 2001. Tectonic contraction across Los Angeles after removal of groundwater pumping effects, *Nature,* **412,** 812–815.

Beauducel, B., Briole, P. & Froger, J.L., 2000. Volcano-wide fringes in ERS synthetic aperture radar interferograms of Etna (1992–1998): deformation or tropospheric effect?, *J. geophys. Res.,* **105,** 16391–16402.

Bennartz, R. & Fischer, J., 2001. Retrieval of columnar water vapour over land from back-scattered solar radiation using the Medium Resolution Imaging Spectrometer (MERIS), *Remote Sens. Env.,* **78,** 271–280.

Bevis, M., Businger, S., Chiswell, S., Herring, T.A., Anthes, R.A., Rocken, C. & Ware, R.H., 1994. GPS Meteorology: Mapping zenith wet delays onto precipitable water, *J. appl. Meteor.,* **33,** 379–386.

Bock, Y. & Williams, S., 1997. Integrated Satellite Interferometry in Southern California, *EOS, Trans. Am. geophys. Un.,* **78**(29), 293, 299–300.

Chaabane, F., Avallone, A., Tupin, F., Briole, P. & Maître, H., 2007. A multitemporal method for correction of tropospheric effects in differential SAR Interferometry: application to the Gulf of Corinth Earthquake, *IEEE Trans. Geosci. Remote Sens.,* **45,** 1605–1615.

Delacourt, C., Briole, P. & Achache, J., 1998. Tropospheric corrections of SAR interferograms with strong topography: application to Etna, *Geophys. Res. Lett.,* **25**(15), 2849–2852.

Ding, X.L., Liu, G.X., Li, Z.W., Li, Z.L. & Chen, Y.Q., 2004. Ground subsidence monitoring in Hong Kong with satellite SAR interferometry, *Photogram. Eng. Remote Sensing,* **70**(10), 1151–1156.

Ding, X.L., Li, Z.W., Zhu, J.J., Feng, G.C. & Long, J.P., 2008. Atmospheric effects on InSAR measurements and their mitigation, *Sensors,* **8,** 5426–5448.

Elsinore basin groundwater advisory committee, 2011. 2010 Elsinore Basin Status Report, 1–68.

Emardson, T.R. & Johansson, J.M., 1998. Spatial interpolation of the atmospheric water vapor content between sites in a ground-based GPS network, *Geophys. Res. Lett.,* **25**(17), 3347–3350.

ESA, 2006. *MERIS Product Handbook,* Issue 2.1. Available at: http://envisat.esa.int/dataproducts/meris (last accessed on 2012 March 15).

Farr, T.G. & Kobrick, M., 2000. Shuttle Radar Topography Mission produces a wealth of data, *EOS, Trans. Am. geophys. Un.,* **81,** 583–585.

Feng, G.C., Hetland, E.A., Ding, X.L., Li, Z.W. & Zhang, L., 2010. Coseismic fault slip of the 2008 Mw 7.9 Wenchuan earthquake estimated from InSAR and GPS measurements, *Geophys. Res. Lett.,* **37,** L01302, doi:10.1029/2009GL041213.

Feng, G.C., Ding, X.L., Li, Z.W., Jiang, M., Zhang, L. & Omura, M., 2011. Calibration of InSAR-derived coseimic deformation map associated with the 2011 Mw 9.0 Tohoku-Oki earthquake, *IEEE Geosci. Remote Sens. Lett.,* **9**(2), 302–306, doi:10.1109/LGRS.2011.2168191.

Ferretti, A., Prati, C. & Rocca, F., 1999. Multibaseline InSAR DEM reconstruction: the wavelet approach, *IEEE Trans.Geosci. Remote Sens.,* **37**(2), 705–715.

Ferretti, A., Prati, C. & Rocca, F., 2000. Nonlinear subsidence rate estimation using permanent scatters in differential SAR interferometry, *IEEE Trans. Geosci. Remote Sens.,* **38**(5), 2202–2212.

Fialko, Y., 2006. Interseismic strain accumulation and the earthquake potential on the southern San Andreas fault system, *Nature,* **441,** 968–971.

Fielding, E.J., Blom, R.G. & Goldstein, R.M., 1998. Rapid subsidence over oil fields measured by SAR Interferometry, *Geophys. Res. Lett.,* **25**(17), 3215–3218.

Foster, J., Brooks, B., Cherubini, T., Shacat, C., Businger, S. & Werner, C., 2006. Mitigating atmospheric noise for InSAR using a high resolution weather model, *Geophys. Res. Lett.,* **33,** L16304, doi:10.1029/2006GL026781.

Fruneau, B. & Sarti, F., 2000. Detection of ground subsidence in the city of Paris using radar interferometry: isolation of deformation from atmospheric artifact using correlation, *Geophys. Res. Lett.,* **27,** 3981–3984.

Fruneau, B., Deffontaines, B., Rudant, J.P. & Le Parmentier, A.M., 2005. Monitoring vertical deformation due to water pumping in the city of Paris (France) with differential interferometry, *Comp. Rend. Geosci.,* **337,** 1173–1183.

Galloway, D.L., Hudnut, K.W., Ingebritsen, S.E., Phillips, S.P., Peltzer, G., Rogez, F. & Rosen, P., 1998. Detection of aquifer system compaction and land subsidence using interferometric synthetic aperture radar, Antelope Valley, Mojave Desert, California, *Water Resour. Res.,* **34**(10), 2573–2585.

Ge, L.L., Chang, H.C. & Rizos, C., 2007. Mine subsidence monitoring using multi-source satellite SAR images, *Photogram. Eng. Remote Sensing,* **73**(3), 259–266.

Goldstein, R.M., 1995. Atmospheric limitations to repeat-track radar interferometry, *Geophys. Res. Lett.,* **22**(18), 2517–2520.

Goldstein, R.M., Zebker, H.A. & Werner, C.L, 1988. Satellite radar interferometry: two dimensional phase unwrapping, *Radio Sci.,* **23**(4), 713–720.

Goovaerts, P., 1997. *Geostatistics for Natural Resources Evaluation,* Oxford University Press, New York, NY.

Hanssen, R., 1998. *Atmospheric Heterogeneities in ERS Tandem SAR Interferometry,* DEOS Report No.98.1, Delft University press, Delft.

Hanssen, R.F., 2001. *Radar Interferometry: Data Interpretation and Error Analysis,* Kluwer Academic Publishers, Dordrecht.

Hooper, A., Zebker, H.A., Segall, P. & Kampes, B., 2004. A new method for measuring deformation on volcanoes and other natural terrains using InSAR persistent scatterers, *Geophys. Res. Lett.,* **31,** L23611, doi:10.1029/2004GL021737.

Hudnut, K.W., Bock, Y., Galetzka, J.E., Webb, F.H. & Young, W.H., 2001. The Southern California integrated GPS network (SCIGN), in *Proceedings of the 10th FIG international symposium on deformation measurements,* March 19–22, Orange, CA, pp. 129–148.

Jiang, M., Li, Z.W., Ding, X.L., Zhu, J.J. & Feng, G.C., 2011. Modeling minimum and maximum detectable deformation gradients of interferometric SAR measurements, *Int. J. Appl. Earth. Obs.,* **13**(5), 766–777.

Lanari, R., Lundgren, P., Manzo, M. & Casu, F., 2004. Satellite radar interferometry time series analysis of surface deformation for Los Angeles, California, *Geophys. Res. Lett.,* **31,** L23613, doi:10.1029/2004GL021294.

Li, Z.W., 2005. Modeling atmospheric effects on repeat-pass InSAR measurements, *Ph.D dissertation*, Hong Kong Polytechnic University, Hong Kong, 143 pp.

Li, Z.H., Muller, J.P. & Cross, P., 2003a. Tropospheric correction techniques in repeat-pass SAR interferometry, in *Proceedings of the FRINGE 2003 workshop,* ESA ESRIN, Frascati, Italy, 2003 December 1–5.

Li, Z.W., Ding, X.L., Liu, G.X. & Huang, C., 2003b. Atmospheric effects on InSAR measurements—A review, *Geomat. Res. Australasia,* **79,** 43–58.

Li, Z.H., Muller, J.-P., Cross, P. & Fielding, E.J., 2005. Interferometric synthetic aperture radar (InSAR) atmospheric correction: GPS, Moderate Resolution Imaging Spectroradiometer (MODIS), and InSAR integration, *J. geophys. Res.,* **110,** B03410, doi:10.1029/2004JB003446.

Li, Z.H., Fielding, E.J., Cross, P. & Muller, J.-P., 2006a. Interferometric synthetic aperture radar atmospheric correction: GPS topography-dependent turbulence model, *J. geophys. Res.,* **111,** B02404, doi:10.1029/2005JB003711.

Li, Z.H., Muller, J.P., Cross, P., Albert, P., Fischer, J. & Bennartz, R., 2006b. Assessment of the potential of MERIS near-infrared water vapour products to correct ASAR interferometric measurements, *Int. J. Remote Sens.,* **27**(2), 349–365.

Li, Z.H., Fielding, E.J., Cross, P. & Muller, J.P., 2006c. Interferometric synthetic aperture radar atmospheric correction: medium resolution imaging spectrometer and advanced synthetic aperture radar integration, *Geophys. Res. Lett.,* **33,** L06816, doi:10.1029/2005GL025299.

Li, Z.W., Ding, X.L, Huang, C., Wadge, G. & Zheng, D.W., 2006d. Modeling of atmospheric effects on InSAR measurements by incorporating terrain elevation information, *J. Atmos. Solar-Terres. Phys.,* **68,** 1189–1194.

Li, Z.W., Ding, X.L., Huang, C., Zou, Z.R. & Chen, Y.L., 2007. Atmospheric effects on repeat-pass InSAR measurements over Shanghai region, *J. Atmos. Solar-Terres. Phys.,* **69,** 1344–1356.

Li, Z.W., Ding, X.L., Chen, W., Liu, G.X., Shea, Y.K. & Emerson, N., 2008a. Comparative study of tropospheric empirical model for Hong Kong region, *Surv. Rev.,* **40**(310), 328–341.

Li, Z.W., Ding, X.L., Huang, C., Zhu, J.J. & Chen, Y.L., 2008b. Improved filtering parameter determination for the Goldstein radar interferogram filter, *ISPRS J. Photogramm. Remote Sens.,* **63**(6), 621–634.

Li, Z.H., Fielding, E.J., Cross, P. & Preusker, R., 2009. Advanced InSAR atmospheric correction: MERIS/MODIS combination and stacked water vapour models, *Int. J. Remote Sens.,* **30**(13), 3343–3363.

Lu, Z. & Danskin, W.R., 2001. InSAR analysis of natural recharge to define structure of a ground-water basin, San Bernardino, California, *Geophys. Res. Lett.,* **28**(13), 2661–2664.

Puysségur, B., Michel, R. & Avouac, J.-P., 2007. Tropospheric phase delay in interferometric synthetic aperture radar estimated from meteorological model and multispectral imagery, *J. geophys. Res.,* **112,** B05419, doi:10.1029/2006JB004352.

Madsen, S.N., Zebker, H.A. & Martin, J., 1993. Topographic mapping using radar interferometry: processing techniques, *IEEE Trans. Geosci. Remote Sens.,* **31,** 246–256.

Massonnet, D. & Feigl, K., 1995. Discrimination of geophysical phenomena in satellite radar interferograms, *Geophys. Res. Lett.,* **22,** 1537–1540.

Massonnet, D. & Feigl, K.L., 1998. Radar interferometry and its application to changes in the earth's surface, *Rev. Geophys.,* **36,** 441–500.

Massonnet, D., Feigl, K.L., Rossi, M. & Adragna, F., 1994. Radar interferometry mapping of deformation in the year after the Landers earthquake, *Nature,* **369,** 227–230.

Onn, F. & Zebker, H.A., 2006. Correction for interferometric synthetic aperture radar atmospheric phase artifacts using time series of zenith wet delay observations from a GOS network, *J. geophys. Res.,* **111,** B09102, doi:10.1029/2005JB004012.

Pierce, R., 1970. Reducing land subsidence in the wilmington oil field by use of saline waters, *Water Resour. Res.,* **6**(5), 1505–1514.

Remy, D., Bonvalot, S., Briole, P. & Murakami, M., 2003. Accurate measurements of tropospheric effects in volcanic areas from SAR interferometry data: application to Sakurajima volcano (Japan), *Earth planet. Sci. Lett.,* **213,** 299–310.

Rosen, P.A., Hensley, S., Joughin, I.R., Li, F.K., Madsen, S.N., Rodriguez, E. & Goldstein, R.M., 2000. Synthetic Aperture Radar Interferometry, *Proc. of the IEEE,* **88**(3), 333–382.

Samsonov, S.V., Tiampo, K.F., Rundle, J.B. & Li, Z.H., 2007. Application of DInSAR-GPS optimization for derivation of fine-scale surface motion maps of Southern California, *IEEE Trans.Geosci. Remote Sensing,* **45**(2), 512–521.

Sandwell, D.T. & Price, E.J., 1998. Phase gradient approach to stacking interferograms, *J. geophys. Res.,* **103**(B12), 30183–30204.

Watson, K.M., Bock, Y. & Sandwell, D.T., 2002. Satellite interferometric observations of displacements associated with seasonal groundwater in the Los Angeles basin, *J. geophys. Res.,* **107**(B4), 2074, doi:10.1029/2001JB000470.

Webley, P.W., Wadge, G. & James, I.N., 2004. Determining radio wave delay by non-hydrostatic atmospheric modeling of water vapour over mountains, *Phys. Chem. Earth,* **29,** 139–148.

Wessel, P. & Smith, W.H.F., 1998. New improved version of the Generic Mapping Tools released, *EOS, Trans. Am. geophys. Un.,* **79,** 579, doi:10.1029/98EO00426.

Wicks, C., Thatcher, W. & Dzuri, D., 1998. Migration of fluids beneath Yellowstone Caldera inferred from Satellite Radar Interferometry, *Science,* **282,** 458–462.

Williams, S., Bock, Y. & Fang, P., 1998. Integrated satellite interferometry: tropospheric noise, GPS estimates and implications for interferometric synthetic aperture radar product, *J. geophys. Res.,* **103**(B11), 27051–27068.

Xu, W.B. *et al*., 2010. Correcting atmospheric effects in ASAR interferogram with MERIS integrated water vapor data, *Chin. J. Geophys.,* **53**(5), 1073–1084 (in Chinese).

Xu, W.B., Li, Z.W., Ding, X.L. & Zhu, J.J., 2011a. Interpolating atmospheric water vapor delay by incorporating terrain elevation information, *J. Geodyn.,* **85**(9), 555–564, doi:10.1007/s00190-011-0456-0.

Xu, W.B., Li, Z.W., Ding, X.L., Wang, C.C. & Feng, G.C., 2011b. Application of small baseline subsets D-InSAR technology to estimate the time series land deformation and aquifer storage coefficients of Los Angeles Area, *Chin. J. Geophys.,* **55**(2), 452–461 (in Chinese).

Zebker, H.A. & Goldstein, R.M., 1986. Topographic mapping from interferometric synthetic aperture radar observations, *J. geophys. Res.,* **91,** 4993–4999.

Zebker, H.A., Rosen, P.A. & Hensley, S., 1997. Atmospheric effects in interferometric synthetic aperture radar surface deformation and topographic maps, *J. geophys. Res.,* **102**(B4), 7547–7563.

SUPPORTING INFORMATION

Additional Supporting Information may be found in the online version of this article:

Table S1. GPS stations used in Figs 3, 5, 7 and 9 for comparisons.

Please note: Wiley-Blackwell are not responsible for the content or functionality of any supporting materials supplied by the authors. Any queries (other than missing material) should be directed to the corresponding author for the article.